

H II REGIONS IN M81 GROUP DWARF GALAXIES

BRYAN W. MILLER¹ AND PAUL HODGE¹

Astronomy Department, University of Washington, Seattle, WA 98195

Received 1993 October 12; accepted 1993 December 1

ABSTRACT

H α images of the H II regions of five members of the M81 Group—Ho I, Ho IX, M81dA, M81dB, and IC 2574—have allowed us to calculate their present star formation rates. The H II regions of the galaxies are normal in both their luminosity functions, which are power laws with shallow slopes (~ -1.4), and in their size distributions, which fit exponentials ($D_0 \sim 50$ pc). However, we find that there is a wide range of star formation activity as measured by the star formation and gas depletion timescales. Present star formation activity ranges from essentially zero for M81dA, which has no detected H II regions, to more active galaxies, such as IC 2574. M81dB appears to be in a burst phase.

Subject headings: galaxies: clusters (M81) — galaxies: photometry — H II regions — stars: formation

1. INTRODUCTION

Previous studies of dwarf and irregular galaxies have shown them to have a wide range of star formation rates and evolutionary histories (Hunter & Gallagher 1985; Kennicutt, Edgar, & Hodge 1989; Hodge 1993). Blue compact dwarfs and H II galaxies can be among the most actively star-forming galaxies, while dwarf spheroidals and some dwarf irregulars, such as DDO 187 and Leo A, have almost no current star formation. Important factors contributing to these differences may include environment (proximity to other galaxies), current degree of interaction, the distribution, amount, and kinematics of the ISM in the galaxy, and galaxy mass. In order to understand the influences of these various factors, it is important to study the properties of as many dwarf galaxies as possible. H α observations are a particularly useful and convenient way of measuring current star formation rates and of studying the properties of H II regions in different environments.

We have extended our previous work on the current star formation rates in Local Group dwarf galaxies (Strobel, Hodge, & Kennicutt 1991; Hodge, Lee, & Kennicutt 1989; Hodge & Lee 1990) out to the M81 Group. Specifically, we report the observations of Ho I, Ho IX, IC 2574, M81dA, and M81dB. The M81 Group is particularly attractive for studying dwarf galaxies. First, it is a fairly rich group with a large population of dwarfs. It is also nearby; Freedman et al. (1994) have determined that $m - M = 27.8$ from *Hubble Space Telescope* (HST) observations of Cepheid variables in M81, and we adopt this distance. Proximity has the advantages that our images will be complete to fairly low flux levels and that stellar populations and the interstellar media can be studied in detail as well. Puche et al. (1992) have done high-resolution H I mapping of the M81 Group dwarf Ho II and have found that the interstellar medium (ISM) is very “frothy,” with many shells and voids, and that the H II regions are found along the walls and intersections of these shells. This has important consequences for galaxy evolution, and more comparisons of the H α and H I distributions of dwarf galaxies are needed.

Global star formation rates from H α fluxes allow us to determine the formation timescale and the gas depletion timescale. The former is basically the star formation rate per unit mass

and is useful for comparing the star formation activity in very different galaxies and for determining whether a galaxy has an above or below average star formation rate at the present time. The gas depletion time indicates how long star formation could continue at the current rate of gas consumption. In addition to these global properties, we look at the properties of the H II region diameter and luminosity distributions in these galaxies. This allows comparisons to be made with previous studies of H II regions in similar dwarf galaxies.

2. OBSERVATIONS

H α and continuum CCD images of Ho I, Ho IX, IC 2574, M81dA, and M81dB were obtained with the KPNO 0.9 m telescope on 1991 December 14 and 15. The H α images were taken through a 38 Å half-power bandwidth interface filter centered on 6569 Å, while the continuum images were taken through a 270 Å bandwidth filter centered on 6092 Å. Integration times for the H α and continuum observations were 2400 seconds and 600 seconds, respectively. Observations of Fiege 34 provided absolute flux calibration. December 15 was not photometric, so fluxes and diameters for M81dB are approximate; these data were calibrated using images of UGC-A 86 taken on both nights. On these nights, we also observed the dwarf galaxies NGC 2537, LGS 3, WLM, UGC-A 86, and EGB 0427 + 63. Details of these observations will be presented in a later paper.

Accurate continuum subtraction and calibration of narrow-band images are vital for proper determination of star formation rates. Our method is straightforward to apply and makes use of all the parameters known about the observations (extinction coefficients, filter response functions, standard star spectra). The method is described in detail in the Appendix. In addition to this standard method, we attempted to match the point-spread functions (PSFs) in the H α and continuum images to get the optimum continuum subtraction (Ciardullo, Tamblyn, & Phillips 1990). This effort was frustrated by strong internal reflections by the continuum filter which made the wings of the PSFs in the two images irreconcilably different. While a concern, this should not have strongly affected the continuum subtraction of the H II regions. The reflections become noticeable only for stars near saturation, and even then they contain much less than 1% of the light of the star. For the standard stars, we used an aperture radius about 8

¹ Visiting Astronomer, Kitt Peak National Observatory, which is operated by AURA, Inc., under contract with the NSF.

times the FWHM of the PSF to make sure that we included all of the light.

These data are supplemented by our previous observations of other M81 Group galaxies. Observations of M81, NGC 2403, NGC 2976, and NGC 2366 were obtained at KPNO with the Carnegie image tube (Kennicutt et al. 1989). Newer observations of H α II are described in more detail in Hodge, Strobel, & Kennicutt (1994), and observations of DDO 53 are described in Strobel, Hodge, & Kennicutt (1990).

Positions of the H II regions were determined by identifying stars from the *HST* Guide Star Catalog (GSC) in the fields and then solving for the plate constants. At least five guide stars were used in each field, so the internal errors are small, a fraction of an arcsecond. The largest uncertainty in the positions comes from the overall uncertainty in defining the GSC reference frame. Coordinates should be correct to approximately 2 arcseconds.

3. IDENTIFICATIONS OF H II REGIONS

Unsubtracted H α and continuum-subtracted H α images of the four galaxies with detected H α emission are shown in Figures 1–4 and 5–8, respectively. The unsubtracted images are useful for identifying the fields and for comparing observations at different wavelengths. As can be seen from the figures, most of the H II regions are well isolated and easy to distinguish. However, as in many late-type galaxies, there are also many loops, arcs, and complexes that make the job of defining the boundaries of the H II regions challenging.

To aid our identification of the H II regions, we enhanced the calibrated H α image using an unsharp masking technique and then used the IRAF package HALPHA to automatically detect most of the H II regions (Phillips 1993). The unsharp masking removes any diffuse H α background and makes it easier to distinguish H II regions in crowded areas. However, because unsharp masking caused the HALPHA tasks to routinely miss very diffuse H II regions that we felt were real, we selected all the boundaries at a particular flux level by hand using the IRAF task POLYPHOT; the HALPHA boundaries were used as guides whenever possible. We consistently selected each emission peak as a separate H II region; this included breaking loops and filaments into components rather than trying to decide the extent of a complex feature. The boundaries from the HALPHA routines, which distinguish H II regions by searching for local maxima above a given threshold, were especially useful for distinguishing regions in crowded areas.

We feel that breaking complexes of H α emission into smaller components both makes interpretation easier and is more astrophysically realistic. Since each peak in a complex probably corresponds to a different source of excitation, the number of H II regions that we select is nearly proportional to the number of exciting sources. This type of treatment also makes it easier to interpret the H II region luminosity and size distributions. Considering a complex as a single H II region can have a significant effect on the luminosity and size distributions. In particular, the slopes of the distributions would be shallower than if each peak is considered a separate H II region.

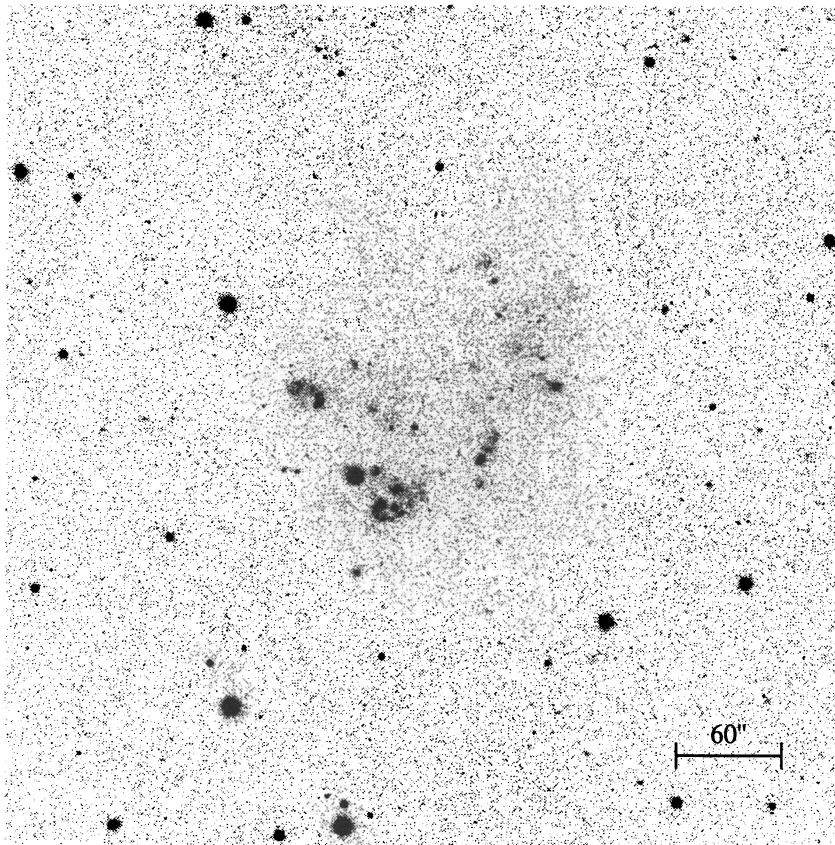


FIG. 1.—Unsubtracted H α image of Ho I. North is up, and east is to the left.

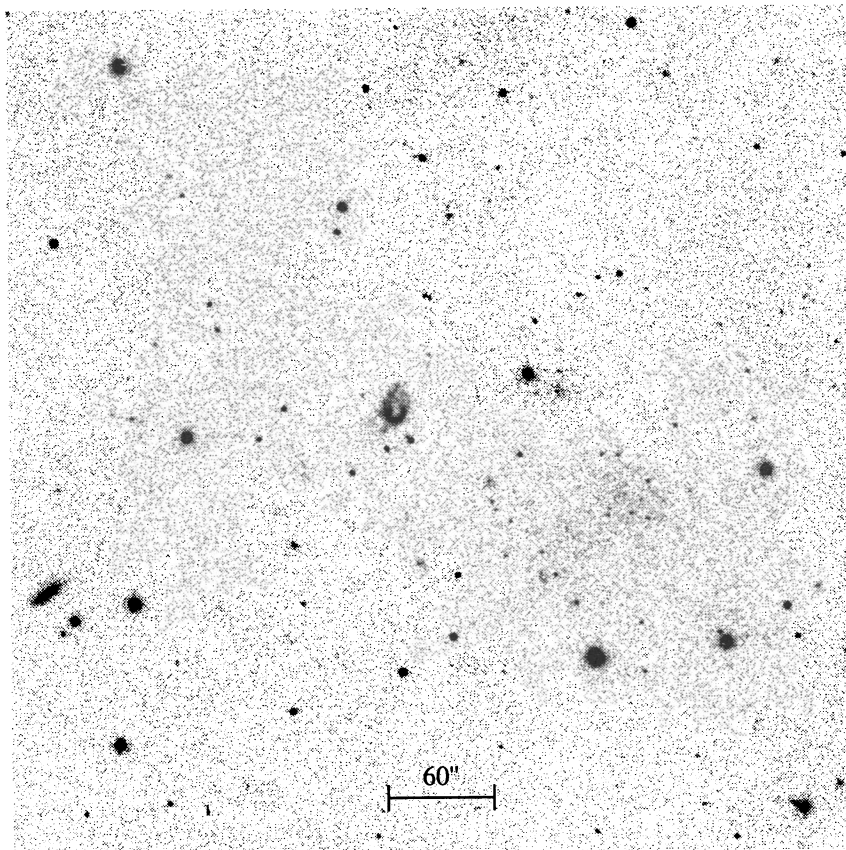


FIG. 2.—Unsubtracted H α image of Ho IX. North is up, and east is to the left.

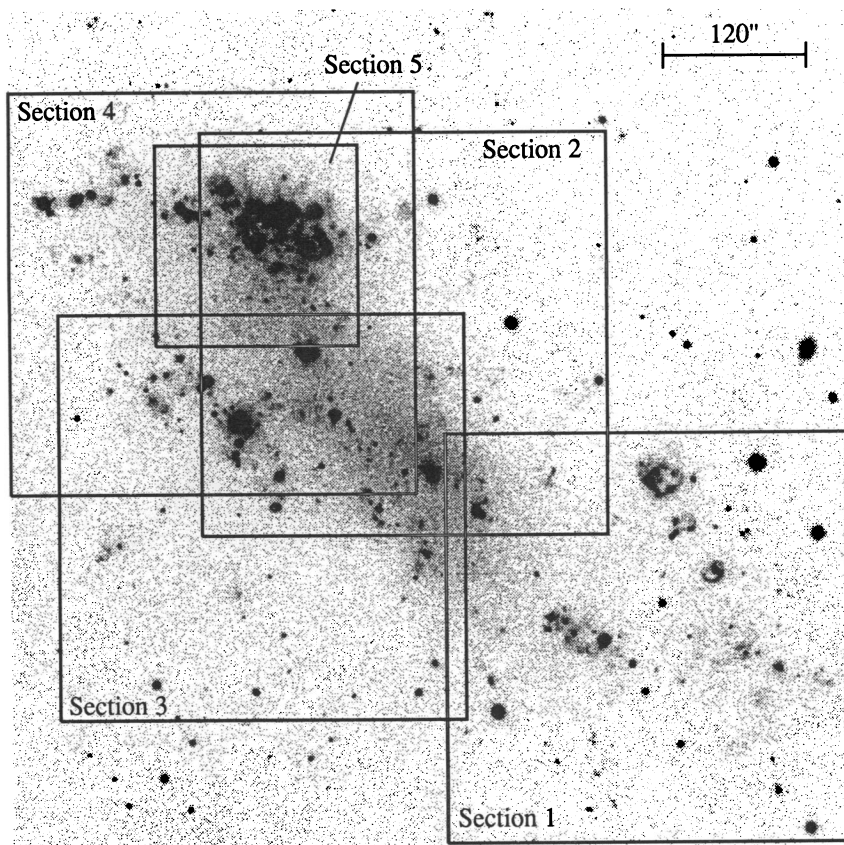


FIG. 3.—Unsubtracted H α image of IC 2574. Sections 1–5 correspond to Figs. 7a–7e, respectively. North is up, and east is to the left.

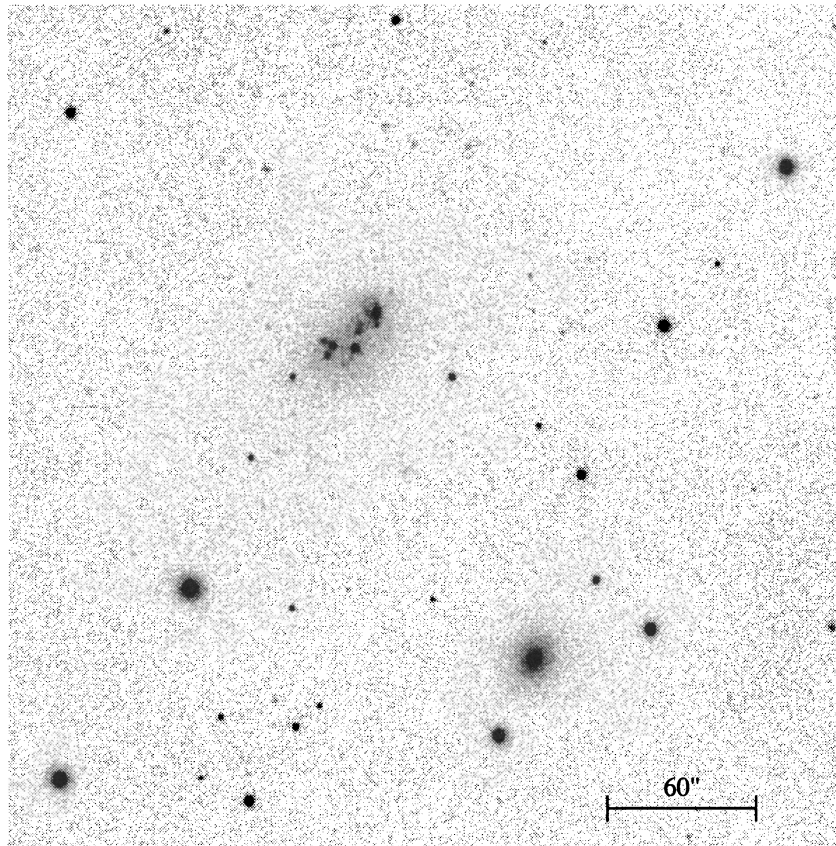


FIG. 4.—Unsubtracted H α image of M81dB. North is up, and east is to the left.

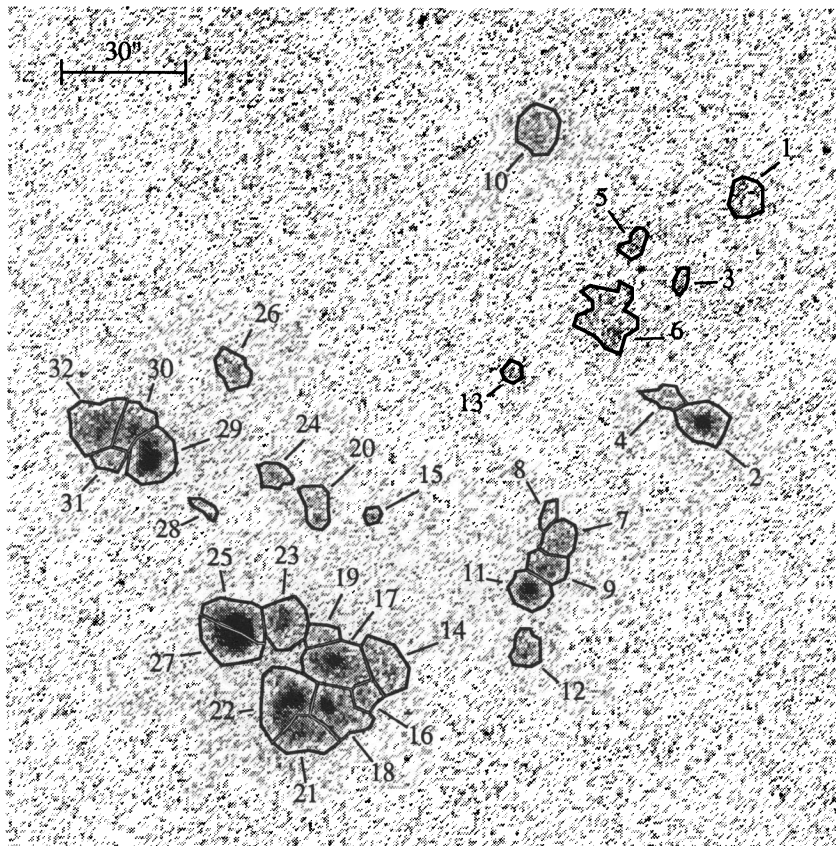


FIG. 5.—Continuum-subtracted H α image of Ho I H II region boundaries and identification numbers (corresponding to MH numbers in Table 1) are shown. North is up, and east is to the left.

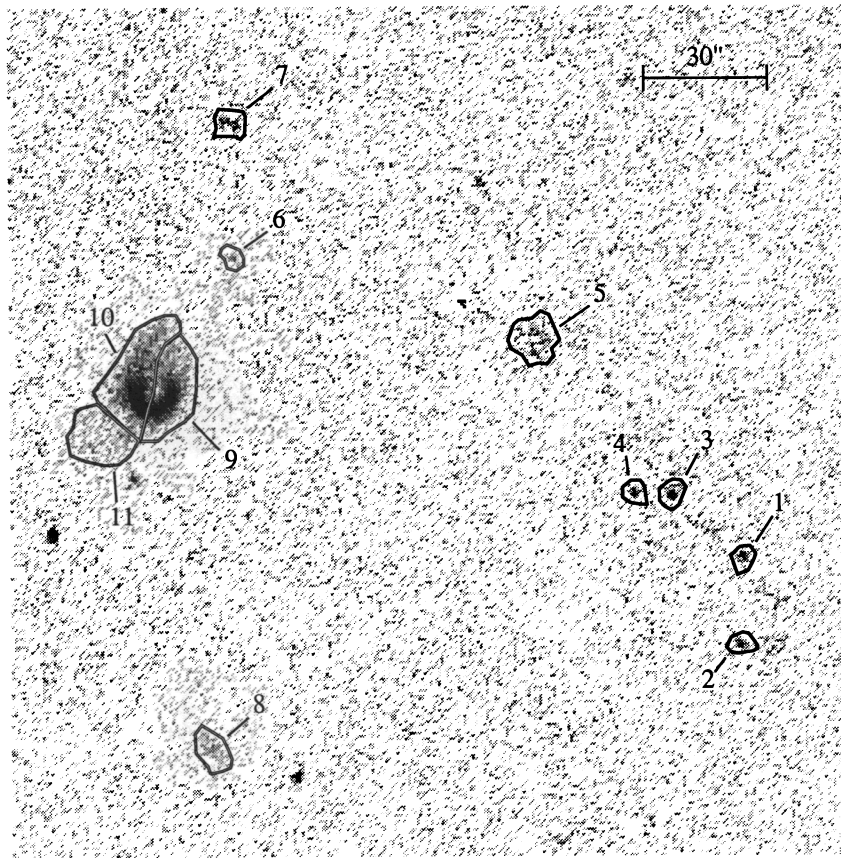


FIG. 6.—Continuum-subtracted $H\alpha$ image of Ho IX. H II region boundaries and identification numbers (corresponding to MH numbers in Table 1) are shown. North is up, and east is to the left.

Furthermore, it is important to treat each H II region population in as consistent a manner as possible so as to make meaningful comparisons among galaxies.

4. $H\alpha$ LUMINOSITIES

For the CCD images, the borders of the H II regions were set at a flux level of approximately 2×10^{-17} ergs sec $^{-1}$ cm $^{-2}$ arcsec $^{-2}$ in the subtracted images. Diffuse $H\alpha$ emission was not very strong, so we have not corrected any of our fluxes for a diffuse component. Also, we have not corrected any of the fluxes for [N II] contamination because abundances are not known for these H II regions. However, as with most low-mass dwarf and Irr galaxies, the nitrogen abundance is probably low so that ignoring the correction probably only introduces an $\sim 5\%$ uncertainty in the flux. Uncertainties in the reported fluxes are probably about 10% due to photometric errors and [N II] contamination. Table 1 gives the coordinates and fluxes of each H II region identified, and Table 2 gives cross-identifications of H II regions in IC 2574 between Hodge & Kennicutt (1983) and this study.

To convert fluxes to luminosities, we had to correct for foreground extinction and distance. For the CCD data, reddenings were taken from Burstein & Heiles (1984) and were converted to magnitudes of extinction at $H\alpha$ by the relation $A_{H\alpha} = 2.32E(B-V)$. We have not corrected for internal extinction since spectra are not available. This lack of correction for internal extinction is probably our largest source of error, and our luminosities should be considered lower limits. Because

Cepheid distances are not known for many of these galaxies, we have adopted the *HST* distance modulus to M81, $m - M = 27.8 \pm 0.2$, for all (Freedman et al. 1994). The random error due to uncertainties in the reddening, the photometry, and the distance is around 15%. The reddenings used and other basic properties of the galaxies from the literature are given in Table 3.

The number of H II regions in each galaxy is given in the second column of Table 4, and the luminosity functions are shown in Figure 9. It is common procedure to fit the differential luminosity functions to the power law

$$N(L) = AL^a dL, \quad (1)$$

which has been shown to be valid for normal galaxies (Kennicutt et al. 1989). The differential luminosity functions in Figure 9 show this to be true in general, especially for the larger galaxies which have more H II regions (see Fig. 9b). All the luminosity functions are plotted with logarithmic bins, and the number of regions in each bin is divided by the bin width so that the slope is parameter a in equation (1). The slopes from weighted least-squares fits to equation (1) are given in Table 4. The weighting is by the square root of number of regions in each bin so that bins with few regions have smaller significance. Both Ho I and IC 2574 show a flattening, or turn-over, in their luminosity distributions at $\log L \sim 36.5$ which is probably due to incompleteness at low luminosities. Therefore, for Ho I, the two lowest luminosity bins were omitted from its fit and the three lowest luminosity bins for IC 2574 were not included in its fit.

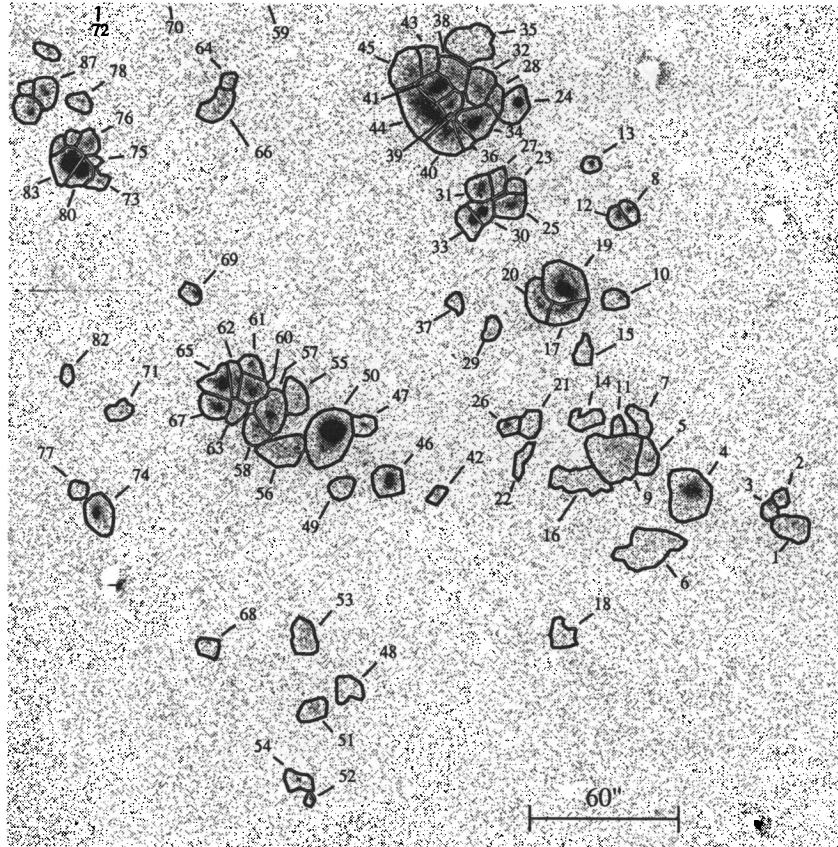


FIG. 7a

FIG. 7.—Continuum-subtracted $H\alpha$ image of IC 2574. H II region boundaries and identification numbers (corresponding to MH numbers in Table 1) are shown. North is up, and east is to the left. (a) Corresponds to Section 1 in Fig. 3; (b) corresponds to Section 2 in Fig. 3; (c) corresponds to Section 3 in Fig. 3; (d) corresponds to Section 4 in Fig. 3; and (e) corresponds to Section 5 in Fig. 3.

In general, the H II region luminosity functions do follow a power law with less luminous galaxies having shallower slopes. For DDO 53, we have rebinned the data from Strobel et al. (1990) after adjusting the luminosities for a distance of 3.63 Mpc. Our value for a in DDO 53, -1.4 ± 0.2 , is slightly lower than, but still consistent with, their value of $-1.9^{+0.3}_{-0.5}$. The large spiral galaxies NGC 3031 and NGC 2403 have the steepest luminosity functions with $a \sim -1.8$. The average slope of the differential luminosity functions for the present sample of dwarf and irregular galaxies is $a = -1.4 \pm 0.4$, which is typical for these types of galaxies (cf. Strobel et al. 1991; Kennicutt et al. 1989).

5. H II REGION DIAMETERS

The second basic property of an H II region population is its diameter distribution. Beginning with van den Bergh (1981), it has been shown that the integral distribution of H II region diameters follows the exponential function

$$N(>D) = N_0 \exp(-D/D_0), \quad (2)$$

where $N(>D)$ is the number of H II regions with diameter larger than D . Also, D_0 appears to be independent of the surface brightness level used to determine the diameter, as long as blending is not a problem (Hodge et al. 1989). We determined an effective diameter for each H II region by using the same areas that were used to measure the fluxes and then

defining $D = 2(A/\pi)^{1/2}$. Cumulative diameter distribution functions for the newly observed galaxies are shown in Figure 10a, and the diameter distributions from some of the other M81 Group galaxies are shown in Figure 10b. In general, the distribution functions are exponential with some noise due to small-number statistics.

The results of unweighted least-squares fits to the linear portions of the diameter distributions are shown in Table 4. Incompleteness is often a problem at small diameters, and we have not included the following points in the fits for the respective galaxies: the four lowest diameter bins for Ho I, the four lowest diameter bins for IC 2574, and the lowest diameter bin for DDO 53. On the high-diameter end, it should be noted that a common feature of irregular galaxies is a large H II region that does not fit on the exponential curve. NGC 2366 is a case in point, and we have omitted from its fit the four highest diameter bins, which are all due to the H II region. Likewise for DDO 53, the highest diameter bin was excluded from its fit. These “giant H II” regions, which are like 30 Doradus, may form by a different process or under different conditions from those for normal H II regions, though a systematic study of this phenomenon is needed. Values for D_0 range between 35 pc and 90 pc and are consistent with scale lengths found for other dwarf galaxies (Strobel et al. 1991; Hodge 1983). Our value of D_0 for DDO 53, 71 ± 5 pc, is slightly higher than but still consistent with the value of 59 ± 6 pc from Strobel et al. (1990).

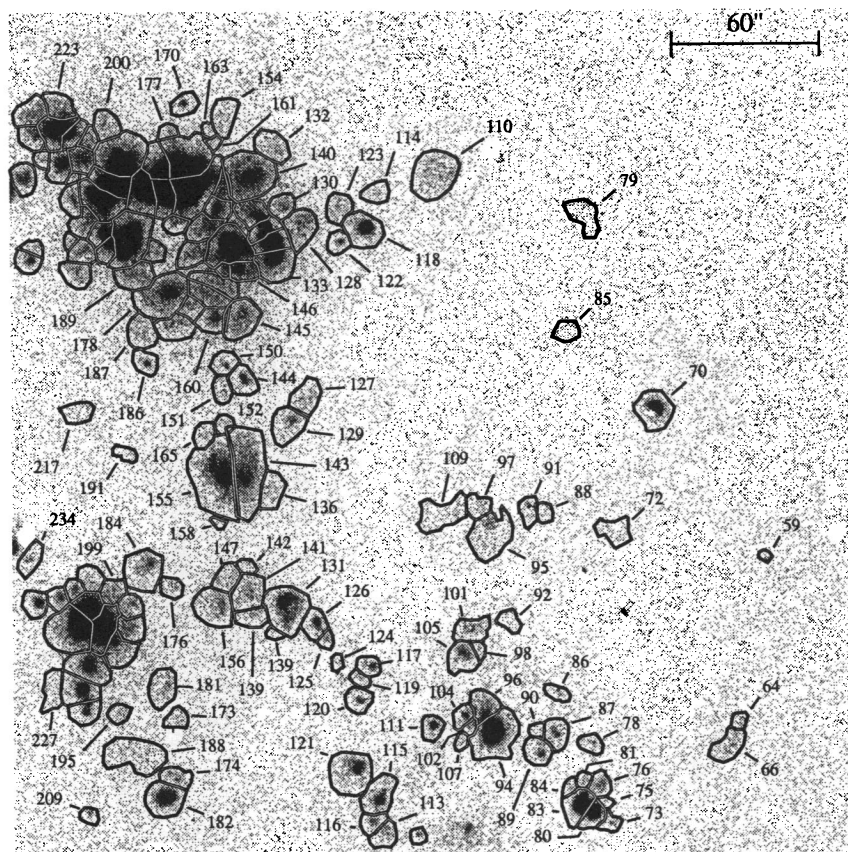


FIG. 7b

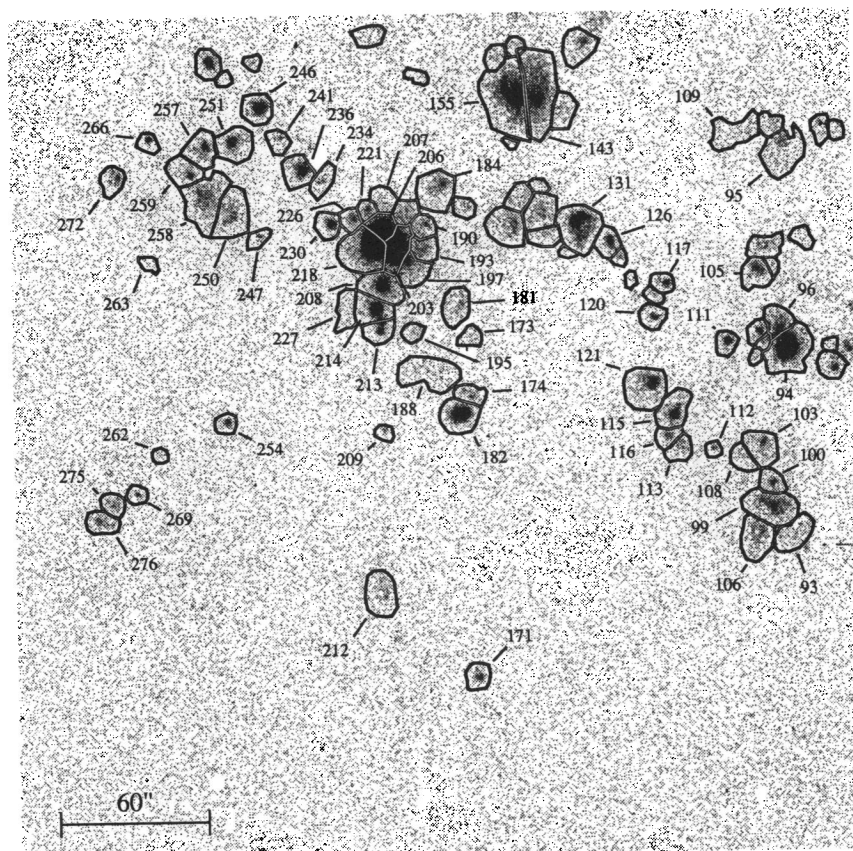


FIG. 7c

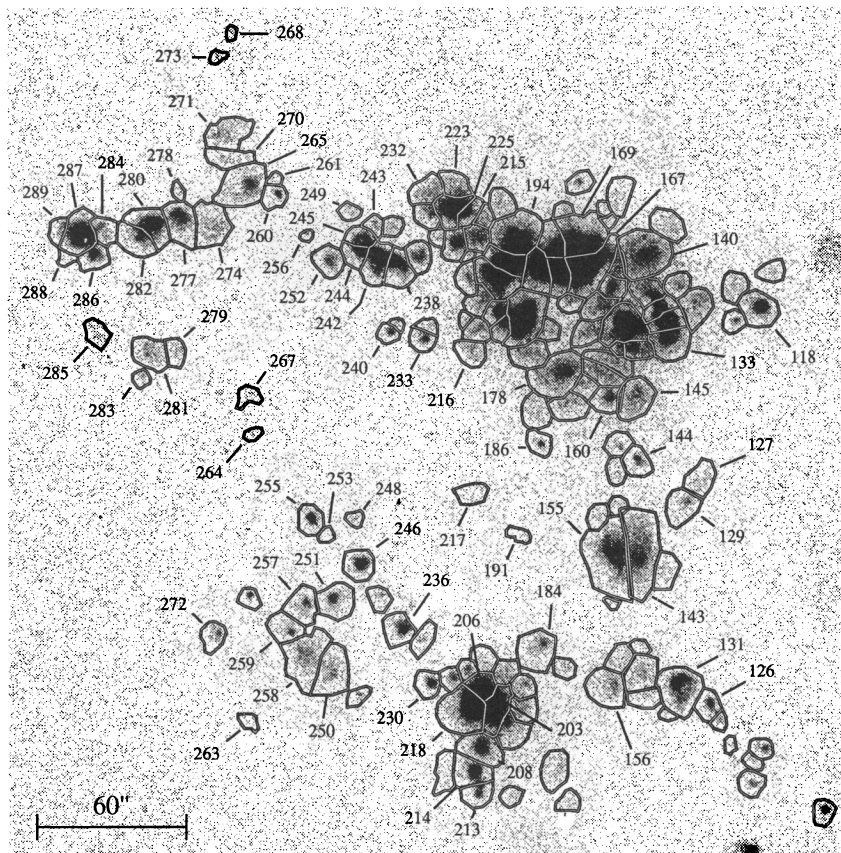


FIG. 7d

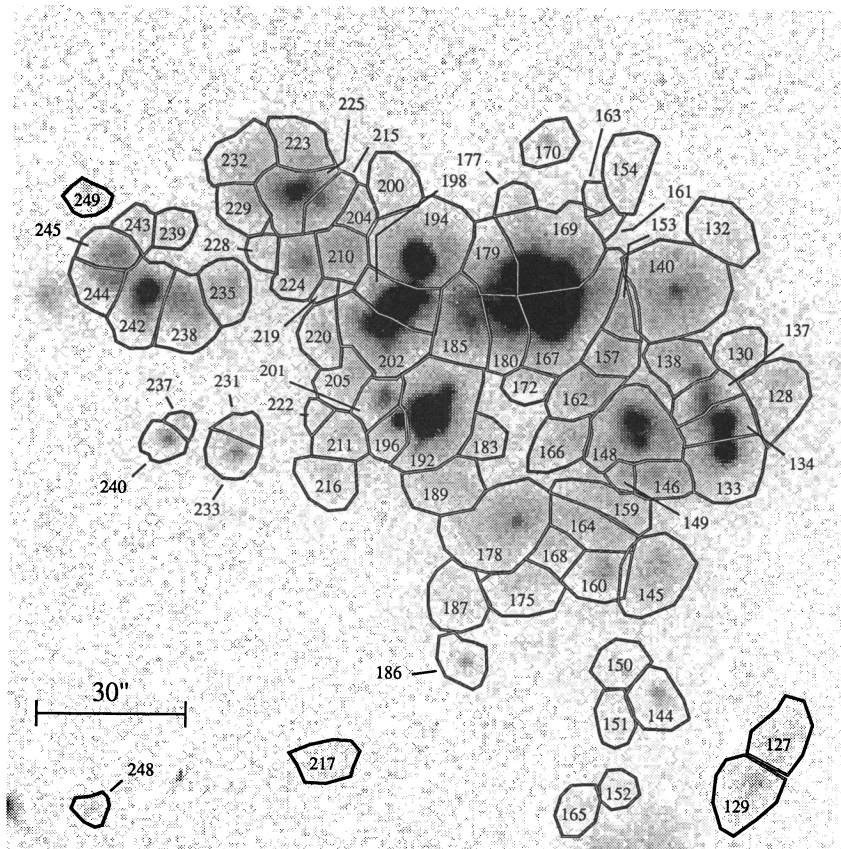


FIG. 7e

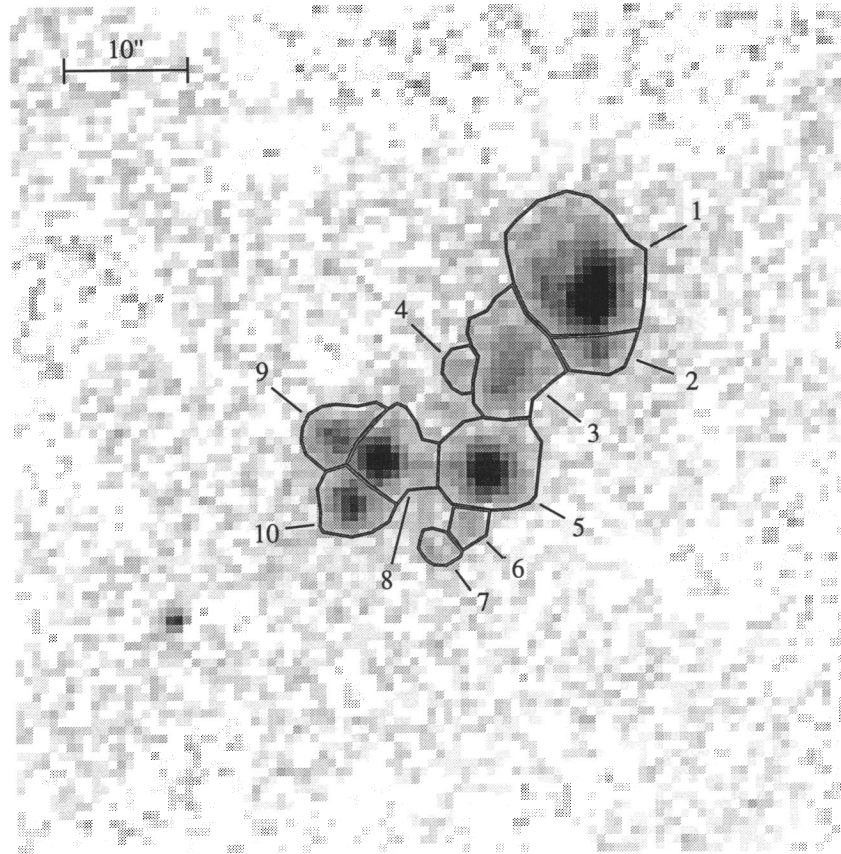


FIG. 8.—Continuum-subtracted $H\alpha$ image of M81dB. H II region boundaries and identification numbers (corresponding to MH numbers in Table 1) are shown. North is up, and east is to the left.

The discrepancy is probably due to the fact that Strobel et al. include the largest H I region in their fit.

The diameter distribution of Ho I is the most discrepant from an exponential. Much of this may be due to incompleteness at small diameters and to small-number statistics at large diameters. However, in contrast to galaxies like NGC 2366, Ho I seems to lack large, luminous H II regions. This is even evident in Figure 1, where it is easy to see that the low surface brightness H II regions are about the same size as the high surface brightness regions. It would be interesting to know the

H I distribution of Ho I in detail to see if conditions in its ISM are very different from those in the other galaxies.

Another important property of the H II regions is their optical morphology, which may be related to conditions in the ISM or to the slope of the initial mass function (IMF). We have followed our past practice of classifying the H II regions with a simple system that provides the reader with a qualitative idea of the morphology of each H II region. These classifications are given in Table 1, and the classification system is described in Hodge & Lee (1990).

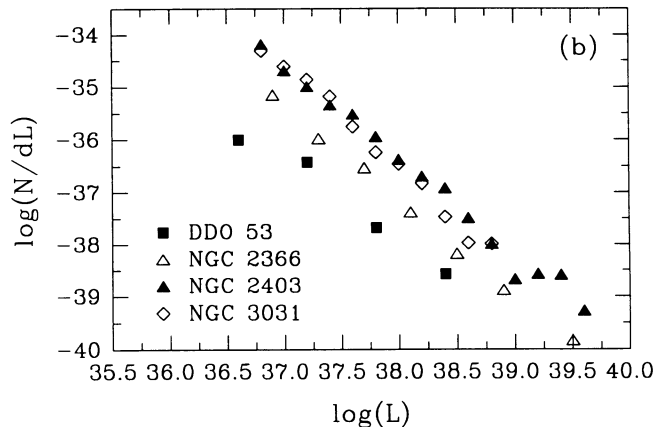
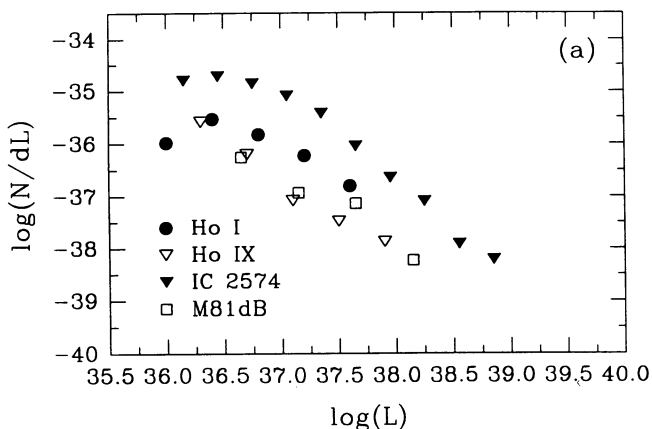


FIG. 9.—H II region luminosity functions for (a) the current sample of dwarf galaxies and (b) other galaxies in the M81 Group, for comparison.

TABLE 1
H II REGIONS IN M81 GROUP DWARF GALAXIES

Number	Coordinate (1950)		Flux ($\times 10^{15}$) erg cm $^{-2}$ s $^{-1}$	Diameter (arcsec)	Morphology Class
	α	δ			
Ho I					
MH 1	09 ^h 35 ^m 45.4	+71°25' 38"	3.48	7.2	d
MH 2	09 35 47.8	+71 24 41	13.35	9.1	b
MH 3	09 35 49.1	+71 25 15	.82	3.6	f
MH 4	09 35 49.8	+71 24 47	2.27	5.6	d
MH 5	09 35 51.3	+71 25 24	1.51	4.9	f
MH 6	09 35 52.2	+71 25 04	7.60	11.0	d
MH 7	09 35 55.3	+71 24 11	4.85	7.1	f
MH 8	09 35 55.9	+71 24 18	1.19	4.3	f
MH 9	09 35 55.9	+71 24 05	5.53	6.8	f
MH 10	09 35 56.3	+71 25 51	6.21	8.8	d
MH 11	09 35 56.8	+71 23 60	10.18	7.6	b
MH 12	09 35 57.0	+71 23 44	3.97	6.4	f
MH 13	09 35 57.7	+71 24 54	1.06	3.9	d
MH 14	09 36 04.2	+71 23 39	6.99	9.1	f
MH 15	09 36 04.9	+71 24 18	1.03	3.2	f
MH 16	09 36 05.4	+71 23 34	3.21	5.7	d
MH 17	09 36 06.8	+71 23 42	19.55	10.7	b
MH 18	09 36 07.2	+71 23 31	17.89	9.9	b
MH 19	09 36 07.4	+71 23 48	2.55	5.5	f
MH 20	09 36 07.7	+71 24 17	3.66	6.8	f
MH 21	09 36 08.6	+71 23 25	11.02	8.7	f
MH 22	09 36 08.9	+71 23 33	26.13	11.4	b
MH 23	09 36 09.4	+71 23 52	9.75	9.2	b
MH 24	09 36 10.0	+71 24 28	2.52	5.5	f
MH 25	09 36 11.7	+71 23 51	26.69	8.8	b
MH 26	09 36 11.9	+71 24 53	3.60	6.8	f
MH 27	09 36 12.0	+71 23 48	20.80	9.2	b
MH 28	09 36 13.3	+71 24 18	1.02	3.8	f
MH 29	09 36 16.4	+71 24 32	25.07	10.0	b
MH 30	09 36 17.2	+71 24 39	8.69	7.7	b
MH 31	09 36 18.3	+71 24 31	2.19	5.4	f
MH 32	09 36 18.9	+71 24 40	13.91	10.4	b
Ho IX					
MH 1	09 ^h 53 ^m 21.7	+69°17' 27"	1.30	4.7	b
MH 2	09 53 22.0	+69 17 04	1.27	4.6	b
MH 3	09 53 25.0	+69 17 42	1.65	5.2	b
MH 4	09 53 26.8	+69 17 42	.99	4.6	b
MH 5	09 53 31.3	+69 18 19	4.32	9.2	d
MH 6	09 53 45.3	+69 18 39	.83	4.4	f
MH 7	09 53 45.5	+69 19 12	1.92	6.0	f
MH 8	09 53 46.4	+69 16 40	2.83	7.3	d
MH 9	09 53 48.3	+69 18 05	27.68	12.9	l
MH 10	09 53 49.9	+69 18 06	36.19	14.7	l
MH 11	09 53 51.8	+69 17 56	6.10	11.5	d
IC 2574					
MH 1	10 ^h 23 ^m 39.2	+68°37' 05"	6.10	10.3	f
MH 2	10 23 40.1	+68 37 16	1.84	5.5	f
MH 3	10 23 40.9	+68 37 12	2.29	5.7	f
MH 4	10 23 46.8	+68 37 18	23.59	15.3	b
MH 5	10 23 49.9	+68 37 31	4.54	8.8	f
MH 6	10 23 50.3	+68 36 55	10.16	15.1	d
MH 7	10 23 50.7	+68 37 48	2.74	7.8	f
MH 8	10 23 51.6	+68 39 14	3.97	6.2	b
MH 9	10 23 52.2	+68 37 35	17.98	16.5	f
MH 10	10 23 52.2	+68 38 38	2.88	7.4	f
MH 11	10 23 52.2	+68 37 46	1.14	5.3	f
MH 12	10 23 52.3	+68 39 11	4.08	6.6	b
MH 13	10 23 54.3	+68 39 33	2.55	5.7	b
MH 14	10 23 54.4	+68 37 47	2.67	8.1	f
MH 15	10 23 54.7	+68 38 15	2.40	7.2	f
MH 16	10 23 55.3	+68 37 22	6.99	12.3	d

TABLE 1—Continued

Number	Coordinate (1950)		Flux ($\times 10^{15}$) erg cm $^{-2}$ s $^{-1}$	Diameter (arcsec)	Morphology Class
	α	δ			
MH 17	10 23 56.2	+68 38 34	11.94	9.5	d
MH 18	10 23 56.5	+68 36 21	2.73	8.4	d
MH 19	10 23 56.4	+68 38 41	54.25	14.0	b
MH 20	10 23 58.3	+68 38 36	9.24	10.0	l
MH 21	10 23 58.9	+68 37 47	2.98	7.9	f
MH 22	10 23 59.5	+68 37 33	2.01	6.8	d
MH 23	10 23 59.8	+68 39 23	2.72	5.7	f
MH 24	10 23 59.8	+68 39 57	16.19	10.2	b
MH 25	10 24 00.3	+68 39 16	9.57	9.4	f
MH 26	10 24 00.7	+68 37 45	3.07	6.4	f
MH 27	10 24 01.4	+68 39 24	3.79	6.9	f
MH 28	10 24 01.6	+68 39 58	4.35	6.8	d
MH 29	10 24 01.9	+68 38 23	2.28	6.4	d
MH 30	10 24 02.5	+68 39 13	14.70	7.7	b
MH 31	10 24 02.6	+68 39 23	9.99	8.8	b
MH 32	10 24 02.8	+68 40 03	12.62	10.6	d
MH 33	10 24 03.2	+68 39 10	12.84	8.4	b
MH 34	10 24 03.3	+68 39 49	26.85	11.1	b
MH 35	10 24 03.3	+68 40 21	8.71	13.6	d
MH 36	10 24 04.2	+68 39 46	5.02	6.0	f
MH 37	10 24 04.6	+68 38 36	1.64	5.5	f
MH 38	10 24 04.9	+68 40 08	11.88	9.9	f
MH 39	10 24 04.9	+68 39 56	8.64	7.4	b
MH 40	10 24 05.3	+68 39 46	16.16	10.3	b
MH 41	10 24 05.7	+68 40 05	32.37	9.6	b
MH 42	10 24 05.9	+68 37 17	1.51	5.3	f
MH 43	10 24 06.7	+68 40 16	6.46	8.1	f
MH 44	10 24 06.7	+68 39 55	47.57	14.5	b
MH 45	10 24 07.9	+68 40 09	11.37	11.5	d
MH 46	10 24 09.5	+68 37 24	13.58	10.2	b
MH 47	10 24 11.5	+68 37 45	3.32	7.4	f
MH 48	10 24 12.2	+68 35 58	3.13	8.6	d
MH 49	10 24 12.8	+68 37 21	3.37	7.5	f
MH 50	10 24 14.0	+68 37 43	139.02	16.9	b
MH 51	10 24 15.1	+68 35 50	4.03	8.3	d
MH 52	10 24 15.4	+68 35 13	.89	3.5	d
MH 53	10 24 15.9	+68 36 18	5.75	9.8	d
MH 54	10 24 16.3	+68 35 20	3.14	7.6	d
MH 55	10 24 16.5	+68 37 57	6.29	9.6	f
MH 56	10 24 17.2	+68 37 35	13.66	12.1	d
MH 57	10 24 18.5	+68 37 49	18.18	11.6	b
MH 58	10 24 19.5	+68 37 45	7.77	8.5	f
MH 59	10 24 19.6	+68 41 13	.70	3.8	f
MH 60	10 24 19.9	+68 37 59	14.60	9.4	b
MH 61	10 24 19.9	+68 38 10	4.64	7.5	f
MH 62	10 24 21.0	+68 38 04	7.01	6.9	f
MH 63	10 24 21.1	+68 37 52	3.89	7.0	d
MH 64	10 24 21.6	+68 40 06	1.96	5.5	f
MH 65	10 24 22.1	+68 38 02	17.79	9.8	b
MH 66	10 24 22.3	+68 39 57	6.62	10.0	d
MH 67	10 24 22.4	+68 37 52	9.88	8.9	b
MH 68	10 24 23.1	+68 36 17	2.19	6.9	f
MH 69	10 24 24.2	+68 38 40	3.52	6.5	f
MH 70	10 24 27.8	+68 42 14	55.40	12.2	b
MH 71	10 24 29.6	+68 37 52	2.95	7.2	f
MH 72	10 24 30.8	+68 41 23	4.17	9.5	d
MH 73	10 24 31.4	+68 39 25	2.31	6.2	f
MH 74	10 24 31.5	+68 37 09	12.58	10.9	b
MH 75	10 24 31.7	+68 39 34	.80	4.2	f
MH 76	10 24 31.9	+68 39 41	5.86	7.6	f
MH 77	10 24 32.4	+68 37 20	1.79	6.0	d
MH 78	10 24 32.6	+68 39 58	3.08	7.0	f

TABLE 1—Continued

Number	Coordinate (1950)			Flux ($\times 10^{15}$) erg cm $^{-2}$ s $^{-1}$	Diameter (arcsec)	Morphology Class
	α	δ				
MH 79	10 24 32.8	+68 43 33		4.10	10.1	d
MH 80	10 24 32.9	+68 39 30		24.64	7.9	b
MH 81	10 24 33.3	+68 39 43		2.01	5.1	f
MH 82	10 24 33.6	+68 38 08		1.30	5.1	f
MH 83	10 24 33.6	+68 39 33		54.38	10.1	b
MH 84	10 24 34.1	+68 39 39		1.89	5.2	f
MH 85	10 24 34.9	+68 42 46		2.13	7.4	d
MH 86	10 24 35.2	+68 40 18		2.36	6.3	f
MH 87	10 24 35.4	+68 40 02		6.74	9.1	f
MH 88	10 24 36.0	+68 41 32		2.02	6.1	f
MH 89	10 24 36.5	+68 39 53		7.19	9.2	f
MH 90	10 24 36.6	+68 40 03		1.57	5.1	f
MH 91	10 24 37.3	+68 41 35		3.66	7.5	f
MH 92	10 24 38.9	+68 40 51		2.19	6.9	f
MH 93	10 24 39.7	+68 38 47		6.70	11.3	d
MH 94	10 24 40.2	+68 40 03		75.76	15.2	b
MH 95	10 24 40.2	+68 41 28		11.89	14.1	d
MH 96	10 24 40.7	+68 40 08		16.19	9.6	f
MH 97	10 24 40.7	+68 41 36		3.86	7.8	d
MH 98	10 24 41.1	+68 40 36		1.85	5.0	f
MH 99	10 24 41.4	+68 38 57		25.69	14.0	b
MH 100	10 24 41.4	+68 39 07		6.51	8.2	f
MH 101	10 24 41.6	+68 40 45		6.52	9.7	f
MH 102	10 24 41.6	+68 40 06		3.38	4.9	f
MH 103	10 24 42.1	+68 39 23		9.99	11.2	f
MH 104	10 24 42.1	+68 40 09		6.96	7.1	f
MH 105	10 24 42.2	+68 40 35		9.87	10.1	f
MH 106	10 24 42.5	+68 38 48		12.51	12.3	d
MH 107	10 24 42.5	+68 39 60		1.16	4.9	f
MH 108	10 24 43.5	+68 39 17		3.28	8.0	d
MH 109	10 24 43.7	+68 41 34		6.69	12.3	d
MH 110	10 24 44.2	+68 43 50		16.61	15.3	d
MH 111	10 24 44.6	+68 40 05		8.91	7.6	b
MH 112	10 24 45.8	+68 39 21		1.88	5.2	f
MH 113	10 24 48.2	+68 39 24		5.11	8.2	f
MH 114	10 24 48.6	+68 43 43		3.01	7.8	f
MH 115	10 24 48.6	+68 39 35		16.39	11.3	b
MH 116	10 24 49.1	+68 39 27		4.82	7.4	f
MH 117	10 24 49.2	+68 40 30		5.21	7.1	f
MH 118	10 24 49.4	+68 43 29		35.89	12.1	b
MH 119	10 24 50.1	+68 40 26		2.10	5.7	f
MH 120	10 24 50.2	+68 40 16		5.22	8.4	f
MH 121	10 24 50.3	+68 39 48		24.40	14.2	b
MH 122	10 24 51.3	+68 43 24		3.99	7.4	f
MH 123	10 24 51.5	+68 43 38		6.13	9.0	d
MH 124	10 24 51.6	+68 40 31		1.02	4.5	f
MH 125	10 24 52.6	+68 40 42		2.35	5.3	f
MH 126	10 24 53.3	+68 40 48		9.84	8.9	b
MH 127	10 24 53.9	+68 42 19		7.30	10.2	d
MH 128	10 24 54.3	+68 43 31		16.22	11.3	f
MH 129	10 24 55.0	+68 42 10		8.75	11.1	f
MH 130	10 24 55.5	+68 43 37		8.58	8.3	f
MH 131	10 24 55.9	+68 40 56		43.06	14.8	l
MH 132	10 24 56.1	+68 44 01		8.31	10.3	d
MH 133	10 24 56.3	+68 43 17		71.10	11.8	b
MH 134	10 24 56.3	+68 43 24		71.43	9.1	b
MH 135	10 24 56.6	+68 40 43		.65	4.4	f
MH 136	10 24 57.0	+68 41 42		5.45	9.6	f
MH 137	10 24 57.0	+68 43 29		32.06	8.2	b
MH 138	10 24 57.4	+68 43 34		29.75	9.5	b
MH 139	10 24 58.1	+68 40 53		4.48	8.2	f
MH 140	10 24 58.2	+68 43 51		78.80	16.4	b

TABLE 1—Continued

Number	Coordinate (1950)		Flux ($\times 10^{15}$) erg cm $^{-2}$ s $^{-1}$	Diameter (arcsec)	Morphology Class
	α	δ			
MH 141	10 24 58.4	+68 41 01	11.31	11.5	f
MH 142	10 24 58.4	+68 41 12	1.41	5.5	f
MH 143	10 24 58.7	+68 41 46	61.68	18.5	b
MH 144	10 24 58.7	+68 42 28	7.77	9.3	b
MH 145	10 24 58.8	+68 42 54	25.88	12.3	f
MH 146	10 24 58.9	+68 43 13	24.55	8.2	f
MH 147	10 24 59.6	+68 41 05	6.05	8.9	f
MH 148	10 24 59.7	+68 43 23	120.93	13.8	b
MH 149	10 24 59.8	+68 43 13	8.43	4.9	b
MH 150	10 24 60.0	+68 42 33	4.74	8.2	f
MH 151	10 25 00.1	+68 42 22	3.86	7.5	f
MH 152	10 25 00.2	+68 42 09	2.80	6.2	b
MH 153	10 25 00.2	+68 43 47	14.57	7.0	f
MH 154	10 25 00.3	+68 44 14	6.15	10.0	f
MH 155	10 25 00.4	+68 41 48	81.04	19.7	b
MH 156	10 25 00.4	+68 40 56	13.35	12.6	l
MH 157	10 25 00.6	+68 43 37	19.76	8.2	b
MH 158	10 25 00.7	+68 41 29	.69	3.9	f
MH 159	10 25 00.7	+68 43 07	18.21	9.6	f
MH 160	10 25 00.8	+68 42 52	16.30	9.5	b
MH 161	10 25 00.9	+68 44 05	1.35	4.5	f
MH 162	10 25 01.0	+68 43 30	22.41	9.5	b
MH 163	10 25 01.1	+68 44 11	1.47	4.7	f
MH 164	10 25 01.2	+68 43 03	21.00	9.8	f
MH 165	10 25 01.4	+68 42 05	3.52	7.5	f
MH 166	10 25 02.4	+68 43 19	15.33	9.2	f
MH 167	10 25 02.5	+68 43 47	502.93	15.1	b
MH 168	10 25 02.7	+68 42 58	7.57	7.4	f
MH 169	10 25 03.0	+68 43 53	313.54	14.9	b
MH 170	10 25 03.0	+68 44 20	4.84	7.9	b
MH 171	10 25 03.6	+68 37 49	6.08	8.4	b
MH 172	10 25 03.7	+68 43 33	6.14	6.8	f
MH 173	10 25 03.8	+68 40 08	3.06	7.0	f
MH 174	10 25 03.9	+68 39 44	5.40	8.2	f
MH 175	10 25 04.0	+68 42 51	10.34	10.4	f
MH 176	10 25 04.0	+68 41 03	3.31	7.2	f
MH 177	10 25 04.1	+68 44 09	2.76	5.7	f
MH 178	10 25 04.1	+68 43 03	55.03	15.3	b
MH 179	10 25 04.3	+68 43 54	79.29	10.0	b
MH 180	10 25 04.5	+68 43 45	108.99	9.7	b
MH 181	10 25 04.6	+68 40 22	7.45	10.7	d
MH 182	10 25 04.6	+68 39 37	29.09	12.0	b
MH 183	10 25 05.1	+68 43 20	6.48	6.8	f
MH 184	10 25 05.8	+68 41 12	13.68	13.0	b
MH 185	10 25 05.9	+68 43 45	90.43	11.5	b
MH 186	10 25 05.9	+68 42 34	5.18	8.0	b
MH 187	10 25 06.1	+68 42 47	7.67	10.4	f
MH 188	10 25 06.3	+68 39 53	11.14	14.7	d
MH 189	10 25 06.7	+68 43 11	18.32	10.6	f
MH 190	10 25 07.0	+68 40 56	7.66	8.2	b
MH 191	10 25 07.1	+68 41 56	1.63	5.9	d
MH 192	10 25 07.4	+68 43 25	412.48	15.4	b
MH 193	10 25 07.8	+68 40 46	11.50	8.8	f
MH 194	10 25 07.9	+68 43 56	191.08	15.1	b
MH 195	10 25 08.0	+68 40 11	2.76	6.6	f
MH 196	10 25 08.5	+68 43 23	32.43	7.2	b
MH 197	10 25 08.5	+68 40 41	16.91	10.1	f
MH 198	10 25 08.6	+68 43 48	167.04	10.1	b
MH 199	10 25 08.7	+68 40 57	9.50	8.3	f
MH 200	10 25 09.1	+68 44 11	7.63	9.1	f
MH 201	10 25 09.1	+68 43 28	24.06	7.6	b
MH 202	10 25 09.1	+68 43 44	129.13	12.4	b

TABLE 1—Continued

Number	Coordinate (1950)			Flux ($\times 10^{15}$) erg cm $^{-2}$ s $^{-1}$	Diameter (arcsec)	Morphology Class
	α	δ				
MH 203	10 25 09.6	+68 40 45		124.88	11.1	b
MH 204	10 25 10.1	+68 44 05		6.91	6.4	f
MH 205	10 25 10.1	+68 43 34		13.94	8.7	f
MH 206	10 25 10.2	+68 40 53		70.82	8.8	b
MH 207	10 25 10.2	+68 41 05		5.35	8.4	f
MH 208	10 25 10.4	+68 40 30		32.87	12.2	b
MH 209	10 25 10.4	+68 39 31		1.78	5.6	f
MH 210	10 25 10.6	+68 43 58		22.11	8.8	b
MH 211	10 25 10.5	+68 43 21		10.08	8.4	f
MH 212	10 25 10.5	+68 38 23		9.66	12.5	d
MH 213	10 25 10.6	+68 40 17		9.93	8.9	b
MH 214	10 25 10.9	+68 40 21		26.55	11.1	b
MH 215	10 25 11.1	+68 44 09		20.54	7.7	b
MH 216	10 25 11.1	+68 43 13		7.55	9.1	f
MH 217	10 25 11.1	+68 42 14		3.50	8.5	d
MH 218	10 25 11.1	+68 40 51		168.56	15.1	b
MH 219	10 25 11.3	+68 43 50		1.61	3.9	f
MH 220	10 25 11.3	+68 43 42		8.53	8.6	f
MH 221	10 25 11.4	+68 41 02		6.54	6.5	b
MH 222	10 25 11.5	+68 43 24		1.93	4.6	f
MH 223	10 25 12.1	+68 44 17		14.18	9.1	f
MH 224	10 25 12.1	+68 43 56		23.53	9.3	b
MH 225	10 25 12.5	+68 44 10		74.18	10.3	b
MH 226	10 25 12.5	+68 40 59		7.21	7.3	b
MH 227	10 25 13.6	+68 40 21		4.83	9.5	f
MH 228	10 25 13.7	+68 43 58		2.68	5.7	f
MH 229	10 25 14.0	+68 44 08		10.66	8.2	f
MH 230	10 25 14.2	+68 40 56		9.96	8.6	b
MH 231	10 25 14.3	+68 43 21		2.52	5.9	f
MH 232	10 25 14.4	+68 44 15		14.19	10.1	f
MH 233	10 25 14.6	+68 43 16		8.88	7.9	b
MH 234	10 25 14.9	+68 41 14		3.83	8.4	f
MH 235	10 25 15.0	+68 43 50		13.28	9.2	b
MH 236	10 25 16.2	+68 41 18		16.35	10.2	b
MH 237	10 25 16.6	+68 43 22		1.16	4.2	f
MH 238	10 25 16.8	+68 43 48		28.71	10.6	b
MH 239	10 25 17.0	+68 44 02		4.00	6.8	f
MH 240	10 25 17.2	+68 43 19		5.39	6.6	b
MH 241	10 25 17.9	+68 41 32		3.27	7.6	f
MH 242	10 25 18.0	+68 43 50		77.24	11.1	b
MH 243	10 25 18.4	+68 44 03		4.01	6.4	f
MH 244	10 25 19.1	+68 43 52		19.78	8.1	b
MH 245	10 25 19.2	+68 43 56		21.50	8.0	b
MH 246	10 25 19.5	+68 41 45		17.37	10.2	b
MH 247	10 25 19.6	+68 40 52		2.38	6.2	
MH 249	10 25 20.2	+68 44 09		2.36	6.3	f
MH 250	10 25 21.5	+68 41 01		13.90	13.5	f
MH 251	10 25 21.6	+68 41 31		13.41	11.8	d
MH 252	10 25 21.9	+68 43 49		10.47	10.0	b
MH 253	10 25 22.1	+68 41 58		1.06	5.0	f
MH 254	10 25 22.1	+68 39 35		4.46	7.0	f
MH 255	10 25 23.2	+68 42 04		11.79	9.1	b
MH 256	10 25 23.5	+68 43 59		.87	4.0	b
MH 257	10 25 23.6	+68 41 29		10.45	11.1	f
MH 258	10 25 23.6	+68 41 09		21.74	15.3	b
MH 259	10 25 24.7	+68 41 17		7.16	10.1	f
MH 260	10 25 25.7	+68 44 16		6.44	8.1	b
MH 261	10 25 26.1	+68 44 21		.99	4.6	b
MH 262	10 25 27.3	+68 39 22		1.40	5.1	f
MH 263	10 25 27.6	+68 40 43		1.38	5.6	f
MH 264	10 25 27.7	+68 42 39		1.15	4.9	d
MH 265	10 25 27.8	+68 44 20		21.86	14.9	d

TABLE 1—Continued

Number	Coordinate (1950)			Flux ($\times 10^{15}$) erg cm $^{-2}$ s $^{-1}$	Diameter (arcsec)	Morphology Class
	α	δ				
MH 266	10 25 27.8	+68 41 32		3.53	6.7	b
MH 267	10 25 27.9	+68 42 54		2.25	6.8	b
MH 268	10 25 29.1	+68 45 23		1.00	4.1	d
MH 269	10 25 29.0	+68 39 05		3.05	6.5	f
MH 270	10 25 29.4	+68 44 30		5.51	10.0	f
MH 271	10 25 29.5	+68 44 41		11.36	12.4	d
MH 272	10 25 30.1	+68 41 17		5.80	8.5	f
MH 273	10 25 30.3	+68 45 12		1.32	4.7	f
MH 274	10 25 30.4	+68 44 02		12.96	13.0	f
MH 275	10 25 30.6	+68 39 01		5.27	7.7	d
MH 276	10 25 31.9	+68 38 55		6.77	9.1	f
MH 277	10 25 32.8	+68 44 06		26.00	12.4	f
MH 278	10 25 33.0	+68 44 17		1.14	4.9	b
MH 279	10 25 33.2	+68 43 12		4.05	7.8	f
MH 280	10 25 35.4	+68 44 04		46.19	11.7	f
MH 281	10 25 35.4	+68 43 11		10.06	11.1	b
MH 282	10 25 35.7	+68 44 01		19.21	11.0	f
MH 283	10 25 35.9	+68 43 02		2.00	5.5	b
MH 284	10 25 39.0	+68 44 02		8.04	8.6	f
MH 285	10 25 39.3	+68 43 17		3.36	8.1	f
MH 286	10 25 39.5	+68 43 51		14.41	9.0	d
MH 287	10 25 40.4	+68 44 00		97.58	12.3	b
MH 288	10 25 41.5	+68 43 49		1.06	5.3	b
MH 289	10 25 41.8	+68 44 02		5.02	6.9	f
M81dB						
MH 1	10 ^h 01 ^m 23 ^s .2	+70°36' 40''		110.75	9.0	b
MH 2	10 01 23.2	+70 36 36		8.54	3.6	b
MH 3	10 01 24.6	+70 36 34		25.06	6.5	b
MH 4	10 01 25.0	+70 36 26		2.51	2.6	b
MH 5	10 01 25.4	+70 36 22		43.10	6.5	f
MH 6	10 01 25.5	+70 36 35		2.81	2.6	f
MH 7	10 01 26.0	+70 36 19		2.26	2.3	f
MH 8	10 01 26.7	+70 36 27		35.17	5.4	b
MH 9	10 01 27.2	+70 36 24		13.52	4.4	b
MH 10	10 01 27.4	+70 36 29		16.81	4.5	b

6. TOTAL STAR FORMATION RATE

After assuming an IMF, it is possible to convert the total H α luminosity to a total current star formation rate (SFR). Assuming a modified Salpeter IMF, Kennicutt (1983) derives

$$\text{SFR (total)} = \frac{L(\text{H}\alpha)}{1.12 \times 10^{41} \text{ ergs s}^{-1}} M_{\odot} \text{ yr}^{-1} \quad (3)$$

for normal disk galaxies. We have applied the same model to our dwarf galaxies. Table 4 shows the total H α luminosity for the galaxies and the SFR that results from equation (3). Uncertainties in the SFRs are dominated by errors in the H α luminosities as described above, so that the SFRs in Table 4 are lower limits with a random uncertainty of about 20%. The current SFRs vary by over three orders of magnitude between Ho IX and NGC 2403 and are a strong function of absolute blue magnitude. The lack of H α emission from M81dA is consistent with the findings of Sargent, Sancisi, & Lo (1983), who did not detect any H β emission from the brighter resolved knots in the center of the galaxy.

It is also informative to compare the current SFR of a galaxy versus its past average rate. One way of doing this (Hodge 1993) is to calculate how long it would take the galaxy to form its current mass of stars at its current SFR, τ_{form} , and to compare that to the Hubble time. So, assuming the galaxies are

coeval and formed a Hubble time ago, τ_{form} for a galaxy should be about 15 Gyr if its SFR is currently at its average rate, only a few Gyr if the galaxy is undergoing a burst of star formation (or has recently formed), or much longer than a Hubble time if it is in a quiescent phase.

We calculate τ_{form} by first calculating the stellar mass of each galaxy from its absolute blue magnitude. Using the apparent blue magnitude—corrected for foreground extinction and inclination—of each galaxy from the RC3 (de Vaucouleurs et al. 1991) and assuming a distance modulus of 27.8 gives the absolute blue magnitudes shown in Table 3. The mass of stars in solar units is then calculated using

$$M_{*} = Y_B \log^{-1} \left(\frac{M_B - C}{-2.5} \right), \quad (4)$$

where $C = 5.48$ (Allen 1973). The mass-to-light ratio, Y_B , is determined from a fit to theoretical values of Y_B versus $(B - V)$ given in Larson & Tinsley (1978) and scaled by a factor of 2 to account for the mass of low-luminosity stars. These models are based on models with a Salpeter IMF and varying birthrates as a function of time. The relation between Y_B and $(B - V)$ is

$$\log(Y_B) = 2.06 \times (B - V) - 0.807. \quad (5)$$

While there is very little scatter in the theoretical points, com-

TABLE 2
CROSS IDENTIFICATION OF H II REGIONS IN IC 2574

HK # ^a	MH #
1	287
2	280,282
3	281
4	nd ^b
5	265
6	252
7	242
8	239
9	238
10	235
11	225
12	nd
13	198,202
14	203,206,218
15	167,169,179,180
16	143,155
17	148
18	nd
19	133,134
20	131
21	118
22	115
23	94
24	80,83
25	nd
26	50
27	44
28	41
29	34
30	24
31	30,33
32	19
33	nd
34	194
35	192
36	182

^a From Hodge & Kennicutt 1983.

^b Not detected.

parison with the empirical data of Nordsieck (1973) indicates that the uncertainty in Y_B , and thus the uncertainty in τ_{form} , is about 50%. Some typical values of Y_B are ~ 0.5 for Ho II and Ho IX, 2.7 for M81dA, and 9.2 for the large spiral NGC 3031. Our results for M_* are given in Table 3, and the corresponding τ_{form} are given in Table 4. There is quite a range of stellar formation times; M81dB and DDO 53 seem to be forming stars the most vigorously, while Ho I, NGC 2976, NGC 3031, and M81dA, in particular, appear to be in a relatively quiescent phase. The rest of the galaxies, however, are forming stars at a fairly average rate.

A complementary timescale to τ_{form} is τ_{gas} , the number of years that the galaxy can continue to form stars at its present rate of gas consumption, calculated ignoring gas recycling or infall. We determine this by taking the total H I mass from the literature (last column of Table 3) and dividing by the SFR. A rough correction for molecular gas and gas recycling would raise the absolute value of τ_{gas} by about a factor of 2 without changing the relative values. All results from the literature are adjusted to a distance of 2.63 Mpc. The results are given in the last column of Table 4. Again, there is a spread in properties. NGC 2976 and M81dB appear to be on the verge of extin-

guishing their star formation, while Ho IX apparently has a substantial potential for future star formation. However, Ho IX is embedded in the tidally disturbed H I envelope surrounding NGC 3031 so that it is uncertain how much gas is associated with Ho IX (Appleton, Davies, & Stephenson 1981). It is likely that the H I mass that we have quoted for Ho IX is higher than the amount actually bound to the galaxy.

7. SUMMARY

We present our results as part of a continuing program to study the current star formation rates and H II region properties of a large sample of M81 Group galaxies. We find:

1. H II region luminosity functions follow a power law with average slope -1.4 , consistent with previous results for other, similar galaxies.

2. The H II region size distributions are exponentials with scale lengths between 35 and 90 pc with an average value near 50 pc. However, some galaxies have unusually large H II regions which do not fit the exponential, and Ho I may have a deficit of large regions.

3. The current star formation rates range over three orders of magnitude. The star formation lifetimes indicate that Ho IX and IC 2574 are forming stars at roughly their average rate, while M81dB and DDO 53 are in a burst phase and Ho I is in a relatively quiescent phase. M81dA has no current star formation.

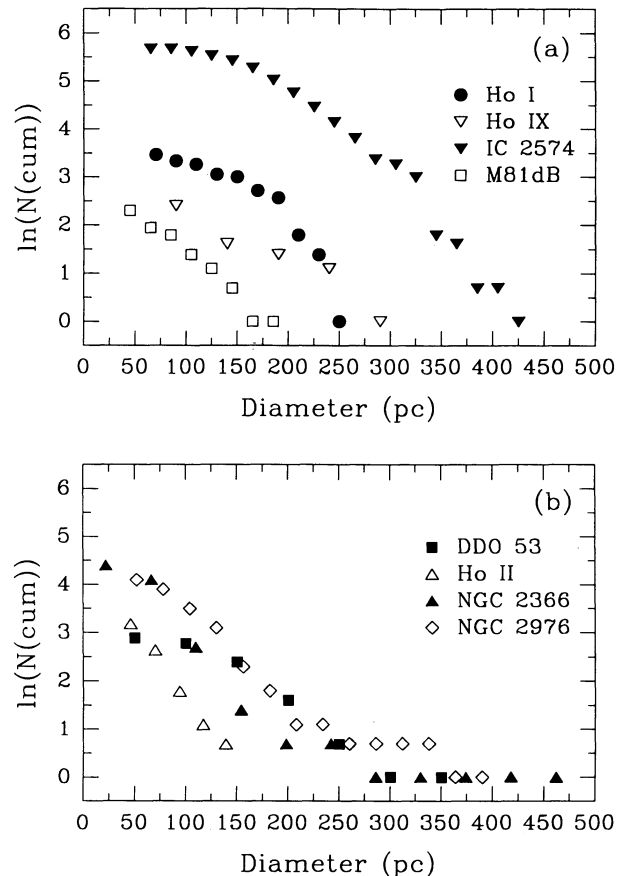


FIG. 10.—H II region cumulative diameter distribution functions for (a) the current sample of dwarf galaxies and (b) other galaxies in the M81 Group, for comparison.

TABLE 3
GENERAL PROPERTIES OF M81 GROUP GALAXIES

Galaxy	$E(B-V)$	B_T^0 ^a	$(B-V)_T^0$ ^b	M_B ^c	$M_*(M_\odot)$ ^d	$M_{HI}(M_\odot)$ ^e
Ho I	0.012	13.01	0.37	-14.8	1.2×10^8	1.4×10^8
Ho IX	0.038	14.08	0.14	-13.7	1.4×10^7	2.5×10^8
IC 2574	0.015	10.33	0.34	-17.5	1.2×10^9	1.3×10^9
M81dB	0.05	14.86	0.25 ^f	-12.9	1.2×10^7	5.6×10^6
M81dA ^g	...	16.5	0.6	-11.3	1.4×10^7	1.4×10^7
DDO 53	...	14.41	0.31	-13.4	2.4×10^7	7.4×10^7
Ho II	...	11.12	0.3 ^h	-16.7	4.7×10^8	7×10^{8i}
NGC 2366	...	11.03	0.45	-16.8	1.0×10^9	8.2×10^8
NGC 2976	...	10.27	0.57	-17.5	4.5×10^9	$< 3 \times 10^7$
NGC 3031	...	7.40	0.86	-20.4	2.1×10^{11}	3×10^9
NGC 2403	...	8.41	0.38	-19.4	8.4×10^9	3.5×10^9

^a Face-on B magnitude corrected for Galactic and external extinction (RC3).

^b Corrected for Galactic and internal extinction and for redshift (except for Ho I) (RC3).

^c Assuming $m - M = 27.8$.

^d Mass is stars.

^e From Huchtmeir & Richter 1989 and adjusted to $D = 3.63$ Mpc, unless noted.

^f From Schmidt et al. 1985.

^g From Sargent et al. 1983.

^h Inferred from Hoessel & Danielson 1984.

ⁱ From Puche et al. 1992.

H α observations of dwarf galaxies are useful for determining their current star formation rates, but they must be augmented with other types of observations if we are to understand the star formation histories and star formation processes in these systems. In particular, high-resolution H I maps would be invaluable for probing the densities and kinematics of the gas in these galaxies and to test Kennicutt's surface-density criteria for star formation (Kennicutt 1989). Spectroscopy of the H II regions is also needed to get oxygen abundances and reddening values. In addition, these galaxies are close enough that the brightest stars are resolved (e.g., Hoessel & Danielson 1984). More studies of the resolved stellar populations in these galaxies need to be done both for determining their star formation

histories and for getting Cepheid distances. Finally, more theoretical work is needed into the evolution of H II regions to see if more physical information can be gleaned from the H II region luminosity and diameter distributions.

We would like to thank Drew Phillips for allowing us to use his IRAF package HALPHA and his unsharp masking technique and for helpful discussions about fitting luminosity functions. We also thank Rob Kennicutt and François Piche for their suggestions on fitting luminosity functions and cumulative distributions, Nick Strobel for his assistance with the continuum subtraction method, and Eric Deutsch for his help with IDL. This research has made use of the NASA/IPAC Extra-

TABLE 4
STAR FORMATION PROPERTIES OF M81 GROUP GALAXIES

Galaxy	N	D_0 (pc)	a	$\log L(H\alpha)$ ^a	SFR ($M_\odot \text{ yr}^{-1}$)	τ_{form} (Gyr)	τ_{gas} (Gyr)
Ho I	32	36 ± 6	-1.0 ± 0.2	38.63	0.004	30	35
Ho IX	11	91 ± 8	-1.5 ± 0.2	38.16	0.001	11	250
IC 2574	289	50 ± 3	-1.8 ± 0.1	39.98	0.08	14	16
M81dB	10	56 ± 3	-1.1 ± 0.2	38.66	0.004	3	1.4
M81dA	0	< 36.1	0
DDO 53	18	71 ± 5	-1.4 ± 0.2	38.78 ^b	0.005	5	14
Ho II	24	36 ± 3	...	39.74 ^c	0.05	10	14
NGC 2366	82	56 ± 6	-1.82 ± 0.07	40.03 ^d	0.10	10	8.5
NGC 2976	61	77 ± 6	...	39.53 ^e	0.03	150	< 1
NGC 3031	524	...	-1.84 ± 0.04	40.18 ^d	0.14	1550	22
NGC 2403	574	...	-1.76 ± 0.03	40.59 ^d	0.35	24	10

^a All luminosities adjusted to $D = 3.63$ Mpc.

^b From Strobel et al. 1990.

^c From Hodge et al. 1993.

^d Calculated from Kennicutt et al. 1989.

^e From Kennicutt & Kent 1983.

galactic Database (NED) which is opened by the Jet Propulsion Laboratory, California Institute of Technology, under contract with the National Aeronautics and Space Adminis-

tration. This work was partially supported by the National Science Foundation through grants INT 91-23283 and AST 92-15821.

APPENDIX

The following method for continuum subtraction and calibration of narrow-band images was originally written up by Myung Gyoon Lee (currently at Seoul National University) at the University of Washington in 1987. Since then, Nick Strobel and one of us (B. W. M.) have added more interpolation options and changed the output format.

The basic procedure of Lee's method is to flux calibrate the line and continuum images based on some simple assumptions about the shape of the nebula's spectrum. Then the continuum can be easily subtracted from the line image. In the following, a subscript l refers to the line passband, a subscript c refers to the continuum passband, a subscript F can refer to either passband, and a superscript s refers to the standard star.

The first step is to determine the extinction coefficients from observation of standard stars. Let the measured counts in the line and continuum be I_l and I_c , respectively. If the exposure times in seconds are T_l and T_c and the sky counts are S_l and S_c , then the measured fluxes are

$$f_c = \frac{I_c - S_c}{T_c}, \quad f_l = \frac{I_l - S_l}{T_l}. \quad (\text{A1})$$

The extinction coefficients in each passband are determined by the slope and intercept of a least-squares fit of standard star instrumental magnitudes versus airmass. The instrumental magnitude outside the atmosphere, $m_{F,0}^s$, is given by

$$m_{F,0}^s = -2.5 \log f_{F,0}^s + C_0 \quad (\text{A2})$$

$$= m_F - k'_F X_F^s + k_F^0, \quad (\text{A3})$$

where $m_F = -2.5 \log f_F^s + C_1$ is the measured instrumental magnitude. The primary extinction coefficient, k'_F (mag per airmass), should always be given as a positive number. The constant terms C_0 , C_1 , and k_F^0 can be ignored so that the flux outside the atmosphere is

$$f_{F,0}^s = f_F^s 10^{0.4k'_F X_F^s}. \quad (\text{A4})$$

Flux calibration consists basically of finding the ratio between count rate and energy flux from the standard star observations. Measured count rates depend on the filter transmission function and the efficiencies of the optics and the detector. The relation between the observed standard star count rate and the absolute energy flux can be expressed as

$$f_{l,0}^s = C_l^s \int_{\lambda_{1l}}^{\lambda_{2l}} \phi_l(\lambda) F_l^s(\lambda) d\lambda, \quad (\text{A5})$$

$$f_{c,0}^s = C_c^s \int_{\lambda_{1c}}^{\lambda_{2c}} \phi_c(\lambda) F_c^s(\lambda) d\lambda, \quad (\text{A6})$$

where $\phi_l(\lambda)$ and $\phi_c(\lambda)$ are the line and continuum filter transmission functions. Substituting from equation (A4), we can solve for the calibration ratios

$$C_l^s = \frac{f_l^s 10^{0.4(k'_F X_F^s)}}{\int_{\lambda_{1l}}^{\lambda_{2l}} \phi_l(\lambda) F_l^s(\lambda) d\lambda}, \quad (\text{A7})$$

$$C_c^s = \frac{f_c^s 10^{0.4(k'_F X_F^s)}}{\int_{\lambda_{1c}}^{\lambda_{2c}} \phi_c(\lambda) F_c^s(\lambda) d\lambda}, \quad (\text{A8})$$

which include corrections for the optical efficiencies of the telescope and detector.

Just as equations (A5) and (A6), we can write the relationship between the observed flux for the program objects and the absolute flux as

$$f_{l,0} = C_l^s \int_{\lambda_{1l}}^{\lambda_{2l}} \phi_l(\lambda) F_l(\lambda) d\lambda, \quad (\text{A9})$$

$$f_{c,0} = C_c^s \int_{\lambda_{1c}}^{\lambda_{2c}} \phi_c(\lambda) F_c(\lambda) d\lambda. \quad (\text{A10})$$

Next we must make some assumptions about the shape of the nebular spectrum. In the simplest case, the emission line has a Gaussian profile and the continuum is flat with respect to wavelength (Fig. 11). The flux per angstrom in the line and continuum are then

$$F_l(\lambda) = \frac{F_l(\text{net})}{\sqrt{\pi}g} \exp \left[-\left(\frac{\lambda - \lambda_0}{g} \right)^2 \right] + F_l(\text{cont}), \quad (\text{A11})$$

$$F_c(\lambda) = \frac{F_c}{\lambda_{2c} - \lambda_{1c}} = \frac{F'_c}{\lambda_{2l} - \lambda_{1l}} = F_l(\text{cont}), \quad (\text{A12})$$

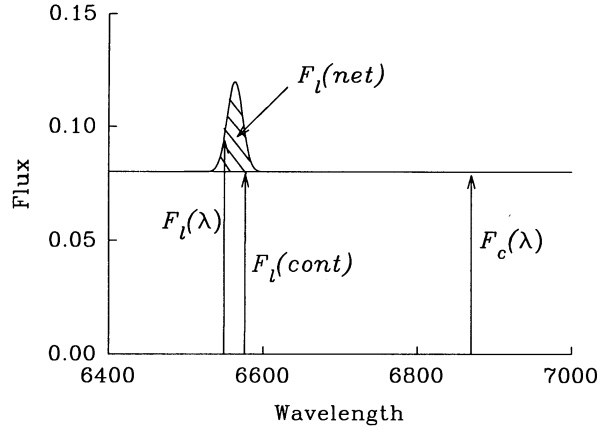


FIG. 11.—A schematic of the assumed shape of the nebular spectrum used in the continuum-subtraction method described in the Appendix. $F_l(\text{cont})$ and $F_c(\lambda)$ are the continuum levels in the line and in the continuum passbands, respectively. $F_l(\lambda)$ is the total flux per angstrom in the line passband. $F_l(\text{net})$ is the total, continuum-subtracted flux of the emission line and is represented by the hatched region.

where $g = \text{FWHM}/[2(\ln 2)^{1/2}]$. Our goal is to solve for $F_l(\text{net})$, the total flux in the line above the continuum. Substituting into equations (A9) and (A10), we find

$$f_{l,0} = C_l^s \int_{\lambda_{11}}^{\lambda_{21}} \phi_l(\lambda) \left[\frac{F_l(\text{net})}{\sqrt{\pi g}} \exp \left[-\left(\frac{\lambda - \lambda_0}{g} \right)^2 \right] + F_l(\text{cont}) \right] d\lambda, \quad (\text{A13})$$

$$f_{c,0} = C_c^s \int_{\lambda_{1c}}^{\lambda_{2c}} \phi_c(\lambda) \frac{F_c}{\lambda_{2c} - \lambda_{1c}} d\lambda = \frac{F_c}{\lambda_{2c} - \lambda_{1c}} C_c^s \int_{\lambda_{1c}}^{\lambda_{2c}} \phi_c(\lambda) d\lambda, \quad (\text{A14})$$

and substituting equation (A14) into equation (A13), using equation (A12),

$$f_{l,0} = F_l(\text{net}) C_l^s \frac{1}{\sqrt{\pi g}} \int_{\lambda_{11}}^{\lambda_{21}} \exp \left[-\left(\frac{\lambda - \lambda_0}{g} \right)^2 \right] \phi_l(\lambda) d\lambda + f_{c,0} \frac{C_l^s \int_{\lambda_{11}}^{\lambda_{21}} \phi_l(\lambda) d\lambda}{C_c^s \int_{\lambda_{1c}}^{\lambda_{2c}} \phi_c(\lambda) d\lambda}. \quad (\text{A15})$$

Let $R = (1/\sqrt{\pi g}) \int_{\lambda_{11}}^{\lambda_{21}} \exp \{ -[(\lambda - \lambda_0)/g]^2 \} \phi_l(\lambda) d\lambda$ and solve for $F_l(\text{net})$,

$$F_l(\text{net}) = \frac{1}{C_l^s R} \left\{ f_{l,0} - f_{c,0} \frac{C_l^s \int_{\lambda_{11}}^{\lambda_{21}} \phi_l(\lambda) d\lambda}{C_c^s \int_{\lambda_{1c}}^{\lambda_{2c}} \phi_c(\lambda) d\lambda} \right\}, \quad (\text{A16})$$

$$F_l(\text{net}) = \frac{1}{R} \left\{ \frac{f_l}{f_l^s} 10^{0.4[k_l(x_l - x_l^s)]} \int_{\lambda_{11}}^{\lambda_{21}} \phi_l(\lambda) F_l^s(\lambda) d\lambda \right. \quad (\text{A17})$$

$$\left. - \frac{f_c}{f_c^s} 10^{0.4[k_l(x_c - x_c^s)]} \frac{\int_{\lambda_{1c}}^{\lambda_{2c}} \phi_c(\lambda) F_c^s(\lambda) d\lambda}{\int_{\lambda_{11}}^{\lambda_{21}} \phi_l(\lambda) F_l^s(\lambda) d\lambda} \frac{\int_{\lambda_{11}}^{\lambda_{21}} \phi_l(\lambda) d\lambda}{\int_{\lambda_{1c}}^{\lambda_{2c}} \phi_c(\lambda) d\lambda} \right\}. \quad (\text{A18})$$

We can write this in a more compact form by letting

$$P = \frac{1}{f_l^s} 10^{0.4[k_l(x_l - x_l^s)]} \int_{\lambda_{11}}^{\lambda_{21}} \phi_l(\lambda) F_l^s(\lambda) d\lambda, \quad (\text{A19})$$

$$Q = \frac{1}{f_c^s} 10^{0.4[k_l(x_c - x_c^s)]} \frac{\int_{\lambda_{1c}}^{\lambda_{2c}} \phi_c(\lambda) F_c^s(\lambda) d\lambda}{\int_{\lambda_{11}}^{\lambda_{21}} \phi_l(\lambda) F_l^s(\lambda) d\lambda} \frac{\int_{\lambda_{11}}^{\lambda_{21}} \phi_l(\lambda) d\lambda}{\int_{\lambda_{1c}}^{\lambda_{2c}} \phi_c(\lambda) d\lambda}, \quad (\text{A20})$$

$$R = \frac{1}{\sqrt{\pi g}} \int_{\lambda_{11}}^{\lambda_{21}} \exp \left[-\left(\frac{\lambda - \lambda_0}{g} \right)^2 \right] \phi_l(\lambda) d\lambda, \quad (\text{A21})$$

so that

$$F_l(\text{net}) = \frac{1}{R} (Pf_l - Qf_c) \quad (\text{A22})$$

$$= \alpha(I_l - \beta I_c + \gamma), \quad (\text{A23})$$

where

$$\alpha = \frac{1}{T_l} \frac{P}{R}, \quad (\text{A24})$$

$$\beta = \frac{T_l}{T_c} \frac{Q}{P}, \quad (\text{A25})$$

$$\gamma = -S_l + S_c \frac{T_l}{T_c} \frac{Q}{P}. \quad (\text{A26})$$

With the final equation, most of the absolute calibration information is contained in parameter α , while the continuum subtraction parameters β and γ should remain constant. Thus, if an improved value of the recessional velocity of the galaxy (which determines λ_0) becomes available, the fluxes can be recalibrated without having to redo the continuum subtraction and without remeasuring the fluxes. Also, applying the flux calibration after measuring the counts in the subtracted images allows you to keep all the information on the photon statistics of the measurements. The other advantages of this method are that it uses minimal approximations and that it uses all the information that is possible to know about an observation.

Using this method, we can also account for multiple emission lines in the line passband. If there are n lines in the passband, then

$$\frac{F_l(\text{net})}{\sqrt{\pi g}} \exp \left[-\left(\frac{\lambda - \lambda_0}{g} \right)^2 \right] \Rightarrow \sum_{i=1}^{n \text{ line}} \frac{a_i F_l(\text{net})}{\sqrt{\pi g}} \exp \left[-\left(\frac{\lambda - \lambda_0^i}{g} \right)^2 \right], \quad (\text{A27})$$

where $\sum_i a_i = 1$ and the flux in line k is $F_l^k(\text{net}) = a_k F_l(\text{net})$. The a_i 's are determined from spectroscopic line ratios.

Others interested in using this method are invited to ask the authors for a copy of the FORTRAN code.

REFERENCES

- Allen, C. W. 1973, *Astrophysical Quantities* (London: Athlone)
- Appleton, P. N., Davies, R. D., & Stephenson, R. J. 1981, *MNRAS*, 195, 327
- Burstein, D., & Heiles, C. 1984, *ApJS*, 534, 33
- Ciardullo, R., Tamblyn, P., & Phillips, A. C. 1990, *PASP*, 102, 1113
- de Vaucouleurs, G., de Vaucouleurs, A., Corwin, Jr., H. G., Buta, R. J., Paturel, G., & Fouque, P. 1991, *Third Reference Catalog of Bright Galaxies (RC3)* (New York: Springer)
- Freedman, W. L., et al. 1994, *ApJ*, in press
- Hodge, P. 1983, *AJ*, 88, 1323
- . 1993, in *Star Forming Galaxies and the Interstellar Medium*, ed. J. Franco, F. Ferrini & G. Tennyson-Tagle (Cambridge: Cambridge Univ. Press), 292
- Hodge, P. W., & Kennicutt, R. C. 1983, *An Atlas of H II Regions in 125 Galaxies* (PAPS Document ANJOA88-296-300) (New York: AIP Auxiliary Publication Service)
- Hodge, P., & Lee, M. G. 1990, *PASP*, 102, 26
- Hodge, P., Lee, M. G., & Kennicutt, R. C. 1989, *PASP*, 101, 32
- Hodge, P., Strobel, N., & Kennicutt, R. C. 1994, *PASP*, submitted
- Hoessel, J. G., & Danielson, G. E. 1984, *ApJ*, 286, 159
- Huchtmeier, W. K., & Richter, O.-G. 1989, *A General Catalog of H I Observations of Galaxies* (New York: Springer)
- Hunter, D. A., & Gallagher, J. S. 1985, *ApJS*, 58, 533
- Kennicutt, R. C. 1983, *ApJ*, 272, 54
- . 1989, *ApJ*, 344, 685
- Kennicutt, R. C., Edgar, B. K., & Hodge, P. W. 1989, *ApJ*, 337, 761
- Kennicutt, R. C., & Kent, S. M. 1983, *AJ*, 88, 1094
- Larson, R. B., & Tinsley, B. M. 1978, *ApJ*, 219, 46
- Nordsieck, K. H. 1973, *ApJ*, 184, 735
- Phillips, A. C. 1993, Ph.D. thesis, Univ. Washington
- Puche, D., Westpfahl, D., Brinks, E., & Roy, J. 1992, *AJ*, 103, 1841
- Sargent, W. L. W., Sancisi, R., & Lo, K. Y. 1983, *ApJ*, 265, 71
- Schmidt, R., Richter, G. M., & Karachentseva, V. E. 1985, *AN*, 306, 4
- Strobel, N. V., Hodge, P., & Kennicutt, R. C. 1990, *PASP*, 102, 1241
- . 1991, *ApJ*, 383, 148
- van den Bergh, S. 1981, *AJ*, 86, 1464